Decoupling of Current Balancing and Reference Tracking Control in Parallel Interleaved Converters

Dejan P. Jovanović, *Member, IEEE*, Mark A. H. Broadmeadow, *Member, IEEE*,
Richard R. Taylor, *Member, IEEE*, Geoffrey R. Walker, *Member, IEEE*,
and Gerard F. Ledwich, *Senior Member, IEEE*

***Abstract*—An attractive approach to increasing the output power and bandwidth of converters is through the parallel connection of multiple, subrated converter cells via mutually coupled inductors. Achieving a balanced contribution to the output current by all paralleled converter cells is critical; good reference tracking performance, however, should also be maintained. Since these two control tasks are coupled, tuning of the controller parameters is challenging. This article demonstrates a methodology for decoupling the output current reference tracking control task from the current balancing control. We show that once balancing and tracking controllers are decoupled, the controller parameter tuning can be conducted independently, simplifying design and analysis of controller performance. Experimental results are presented, which validate the proposed methodology, applied to a three-cell, parallel interleaved converter with cyclic cascade coupled inductor filter network, operating at 100 $\mathrm{V_{RMS}}$ and 9 $\mathrm{A_{RMS}}$.**

***Index Terms*—Balancing, coupled inductors, current sharing, interleaving, paralleling.**

I. INTRODUCTION

THERE is a continual demand for higher power ratings in power electronic converters, driven by application requirements. A common strategy for achieving higher power ratings is through the use of multiple, subrated converter modules, with each converter module contributing one or more cells to an overall converter topology. Where high output currents are required, the parallel connection of converter cells is an attractive topological option. This topology is typically realized using multiple voltage source inverter (VSI) modules connected to a common dc bus [1]–[3], each of which contribute one or more cells to the converter topology (depending on the number of phase legs present in each module). Inductors are used to connect each cell to the point of common connection (PCC), providing decoupling of the instantaneous output voltage state of each cell from both the PCC and other cells (see Fig. 1).

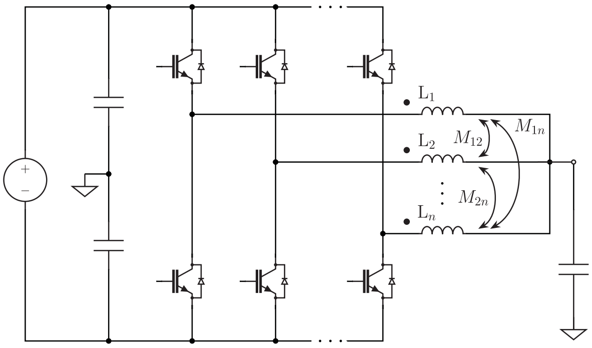

Fig. 1. General n-cell paralleled interleaved converter topology, comprising half-bridge VSI cells coupled to a PCC via phase-leg inductors with mutual coupling.

In addition to the general increase in the total processed power, paralleled converter cells can provide a range of additional benefits, including sharing of semiconductor device current, reduction of harmonic distortion, reduction in the required output filter reactance, and improved control bandwidth [1], [4]–[6]. These topologies have been demonstrated in a number of applications including unity power factor rectification [2] and wind turbines [7]. The inclusion of magnetically coupled inductors can provide further benefits in terms of reduction of the ripple current presented to the semiconductor devices and reduction in the size required for the inductor magnetic cores [8].

It is desirable to achieve a balanced contribution to the output current from all converter cells in order to minimize circulating currents and the required rating of converter components [1]. This sensitivity to current imbalance is a key disadvantage of the paralleling strategy, resulting in a requirement to manage current imbalance and minimize circulating current between cells [7], [9]. It is critical to achieve good current balancing dynamics in order to avoid possible saturation of the inductor magnetic cores that may result from unbalanced cell current. It is equally desirable, however, to achieve optimal dynamics for the reference tracking control for application performance.

A number of control strategies are proposed in the existing literature for the management of current imbalance in paralleled

---

Manuscript received March 20, 2019; revised June 11, 2019; accepted August 6, 2019. Date of publication August 21, 2019; date of current version January 10, 2020. This work was supported by the Defence Science and Technology (DST) Group. Recommended for publication by Associate Editor M. Rodriguez. *(Corresponding author: Mark A. H. Broadmeadow.)*

The authors are with the Queensland University of Technology, Brisbane, QLD 4000, Australia (e-mail: dejan.jovanovic@qut.edu.au; mark.broadmeadow@qut.edu.au; rr.taylor@qut.edu.au; geoffrey.walker@qut.edu.au; g.ledwich@qut.edu.au).

Color versions of one or more of the figures in this article are available online at http://ieeexplore.ieee.org.

Digital Object Identifier 10.1109/TPEL.2019.2936858

See http://www.ieee.org/publications_standards/publications/rights/index.html for more information.

topologies. Typically these utilize an average current-sharing control strategy, which relates the cell, common mode, and differential mode currents [10]. Most commonly, the reference tracking and current balancing control tasks are addressed via a single, combined controller featuring one or more proportional-integral, or proportional-resonant blocks [5], [9], [11]–[15]. A conventional nested control structure featuring an inner and outer loop is used by the work presented in [11]–[15], where one loop is used for reference tracing (voltage or current) and the second loop is used for current balancing.

While these techniques have been shown to be effective in practice, controller parameters must be tuned and do not allow for the dynamic response of the converter reference tracking to be set independently of the balancing dynamic response. Consequently, as the dynamics of current balancing are often much faster than the dynamics of the reference tracking problem, treating the corresponding control tasks as a single, coupled problem can compromise the dynamic performance of one, or both, of these subsystems.

Alternative methods are also presented in the literature. A robust feedback control strategy is presented in [16], in which output voltage tracking and current balancing controllers are coupled by the formulation of the control problem, such that the dynamics of the current balancing controller cannot be designed independently. Decoupling of balancing and reference tracking control is claimed in [17], however, the analysis presented is applicable only to a first-order system, and does not consider the effect of coupled output inductors. Additionally, the balancing control structure proposed in this simulation study results in an asymmetric balancing response across the three phases. In [1], conditional decoupling of the balancing control action from the common mode cell output voltage is demonstrated for a specialized case, however, the dead-beat strategy proposed does not allow the dynamics of the balancing controller to be designed, and this approach is inherently sensitive to system parameter variations.

In this article, we demonstrate decoupling of the overall control problem into two separate, simpler control problems; namely, cell current balancing and converter reference tracking. This methodology overcomes the limitations of existing control strategies by permitting the current balancing and reference tracking controllers to be independently designed and analyzed. Consequently, the proposed methodology provides significant advantages, as the control features and dynamics can be well matched to the characteristics of the two different control tasks, and the performance of both subsystems is directly determinable from standard control design techniques.

This article is organized as follows. Section II describes the paralleled interleaved converter topology to which the decoupling methodology proposed in this article is applied. The proposed decoupling methodology is presented in Section III, and the properties of the resulting decoupled model are examined in Section III-C, including conditions for stability, controllability, and observability. Application of the decoupled model to the independent design of reference tracking and balancing controllers is demonstrated in Section IV, with the decoupled nature of the designed controllers validated experimentally in Section V. Final conclusions are presented in Section VI.

II. Paralleled Interleaved Inverters Utilizing Coupled Inductors

The rationale for the use of paralleled converter topologies has been briefly described in Section I. The decoupling methodology presented in this article will be applied to the general case where mutual coupling may be introduced between the phase-leg inductors of paralleled converter cells. This section describes the salient features of this topology class.

The benefits of coupling the output inductors of VSI cells include an ability to limit the circulating currents, decouple the common mode current from differential mode current, and reduce total current ripple [10]. Coupling of output inductors also produces a multilevel voltage waveform (which appears across the leakage inductance of the phase-leg inductors) where the number of levels depends on the number of paralleled cells [18]. A general representation of the paralleled interleaved converter topology is shown in Fig. 1, where n converter cells are parallel connected to the PCC by phase-leg inductors, which are mutually coupled to the phase-leg inductors of one or more parallel cells.

The leakage inductance in each phase leg decouples the instantaneous phase-leg voltage from the average voltage at the PCC, eliminating the need for precise matching of switching instants between paralleled cells [19]. Furthermore, this affords the opportunity to phase shift the switching instants of each phase leg of the inverter. The greatest performance benefit is achieved when the switching instants are interleaved and equally distributed across the switching period. The major advantage of this configuration is cancelation of the low-order switching frequency harmonics and related ripple components at the output of the converter. The use of coupled inductors can provide the additional benefit of reducing the ripple current presented to each converter cell. With appropriate modulation, interleaving also permits extension of the effective bandwidth of the converter.

While the configuration shown in Fig. 1 demonstrates a general case for a parallel interleaved converter with mutually coupled inductors, in practice, symmetrical mutual coupling between multiple inductors is challenging to achieve, and requires complex magnetic structures. Symmetric coupled inductor networks can be more conveniently constructed from multiple two-winding coupled inductors, otherwise known as inter-cell transformers (ICTs). Examples of common topologies include the cyclic cascade, whiffletree, and combinatorial cascade [10]. These configurations are extensively studied in the literature [1], [8], [10], [18], [20]. For all of these topologies, an equivalent circuit may developed of the form shown in Fig. 1. The resulting equivalent state space model can subsequently be used for the analysis and development of current balancing techniques.

III. Decoupling Methodology

In this section, we present a methodology to decouple the reference tracking and current balancing control problems for paralleled interleaved converters. The coupled problem is defined in Section III-A and the decoupling procedure is subsequently demonstrated in Section III-B. Finally, the properties of the decoupled model are examined in Section III-C.

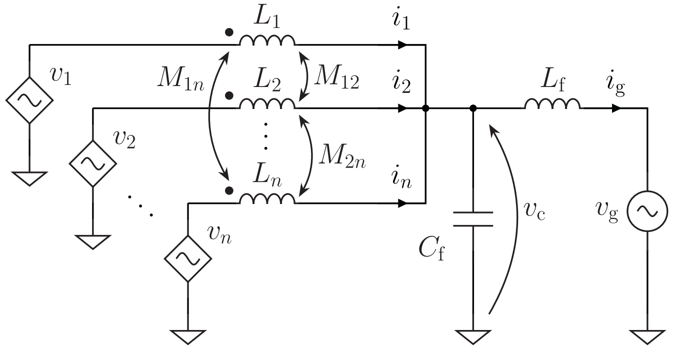

Fig. 2. Equivalent circuit for a symmetrical, n-cell parallel interleaved converter with *LCL* output filter comprising phase-leg inductors with mutual coupling.

A. Problem Formulation

The equivalent circuit for an n-cell paralleled interleaved converter is shown in Fig. 2, with the load modeled as a voltage source connected to the PCC via linking impedance L_f. VSI phase-leg outputs are modeled by voltage sources: $v_1 \ldots v_n$. A general lumped parameter model is used to represent the coupled inductor network, which connects the VSI phase legs to the PCC. For each phase leg, L represents the self-inductance and R is the equivalent series resistance (ESR) of the phase-leg inductor, while M_{jk} represents the mutual inductance between the jth and kth phase-leg inductors. C_f is the filter capacitance at the PCC, and L_f is an inductor with ESR of R_f, which connects the PCC to the load.

A state space model for the equivalent circuit described earlier has the following implicit form:

$$\boldsymbol{E}\dot{\boldsymbol{x}} = \bar{\boldsymbol{A}}\boldsymbol{x} + \bar{\boldsymbol{B}}\boldsymbol{u} \tag{1}$$

where $\boldsymbol{x} \in \mathbb{R}^{(n+2)\times 1}$ and $\boldsymbol{u} \in \mathbb{R}^{(n+1)\times 1}$ are the state-space and control input vectors, which are defined as

$$\boldsymbol{x} = \begin{bmatrix} i_g & v_c & i_1 & i_2 & \ldots & i_n \end{bmatrix}^{\mathsf{T}} \tag{2}$$

$$\boldsymbol{u} = \begin{bmatrix} v_g & v_1 & v_2 & \ldots & v_n \end{bmatrix}^{\mathsf{T}}. \tag{3}$$

The matrices $\boldsymbol{E}$, $\bar{\boldsymbol{A}}$, and $\bar{\boldsymbol{B}}$ are given as

$$\boldsymbol{E} = \left[\begin{array}{cc|c} L_f & 0 & \\ 0 & C_f & \\ \hline & & \boldsymbol{\mathcal{L}} \end{array}\right] \tag{4}$$

$$\bar{\boldsymbol{A}} = \left[\begin{array}{cc|c} -R_f & 1 & \boldsymbol{0}_{1\times n} \\ -1 & 0 & \boldsymbol{1}_{1\times n} \\ \hline \boldsymbol{0}_{n\times 1} & -\boldsymbol{1}_{n\times 1} & -R\cdot \boldsymbol{I}_{n\times n} \end{array}\right] \tag{5}$$

$$\bar{\boldsymbol{B}} = \left[\begin{array}{c|c} -1 & \\ 0 & \\ \hline & \boldsymbol{I}_{n\times n} \end{array}\right] \tag{6}$$

where $\boldsymbol{0}_{p\times q}$ and $\boldsymbol{1}_{p\times q}$ are $p \times q$ dimension matrices of zeros and ones, respectively, where undefined matrix partitions have all elements set to zero. $\boldsymbol{\mathcal{L}} \in \mathbb{R}^{n\times n}$ is the coupling matrix, which for the case of a symmetrical coupling network takes the form of a circulant matrix. $\boldsymbol{\mathcal{L}}$ is defined in the Appendix for the uncoupled, multicoupled, whiffletree, combinatorial cascade, and cyclic cascade coupling networks. In order to have an explicit state-space representation of the model (1), an inverse of matrix $\boldsymbol{E}$ is required. The inverse of matrix $\boldsymbol{E}$ is

$$\boldsymbol{E}^{-1} = \left[\begin{array}{cc|c} L_f^{-1} & 0 & \\ 0 & C_f^{-1} & \\ \hline & & \boldsymbol{\mathcal{L}}^{-1} \end{array}\right]. \tag{7}$$

As $\boldsymbol{\mathcal{L}}$ is strictly diagonally dominant (see Appendix), $\boldsymbol{\mathcal{L}}^{-1}$ and consequently $\boldsymbol{E}^{-1}$ are guaranteed to exist.

The explicit form of the model (1) is obtained by multiplying the equation on the left-hand side (LHS) by $\boldsymbol{E}^{-1}$. Following this transformation, the state-space model has the following recognizable, explicit form

$$\dot{\boldsymbol{x}} = \boldsymbol{A}\boldsymbol{x} + \boldsymbol{B}\boldsymbol{u} \tag{8}$$

where

$$\boldsymbol{A} = \boldsymbol{E}^{-1}\bar{\boldsymbol{A}} = \left[\begin{array}{cc|c} -R_f L_f^{-1} & L_f^{-1} & \boldsymbol{0}_{1\times n} \\ -C_f^{-1} & 0 & C_f^{-1}\cdot \boldsymbol{1}_{1\times n} \\ \hline \boldsymbol{0}_{n\times 1} & -\gamma\cdot \boldsymbol{1}_{n\times 1} & -R\cdot \boldsymbol{\mathcal{L}}^{-1} \end{array}\right] \tag{9}$$

$$\boldsymbol{B} = \boldsymbol{E}^{-1}\bar{\boldsymbol{B}} = \left[\begin{array}{c|c} -L_f^{-1} & \\ 0 & \\ \hline & \boldsymbol{\mathcal{L}}^{-1} \end{array}\right] \tag{10}$$

and the coefficient γ is defined as the row sum of $\boldsymbol{\mathcal{L}}^{-1}$ such that

$$\gamma = \sum_{i=1}^{n} l_i, \quad \boldsymbol{\mathcal{L}}^{-1} = \mathrm{circ}\left(l_1, l_2, \ldots, l_n\right) \tag{11}$$

where the circ operator produces a circulant matrix with first row equal to the operand.

Inspection of matrices $\boldsymbol{A}$ and $\boldsymbol{B}$ shows that the model states are coupled. In other words, any change of a state directly affects other states, and vice versa. As a specific example, a change to state v_c would affect states $i_1 \ldots i_n$. This implies the need to tune the cell current balancing controller to also compensate for load disturbances, significantly complicating controller design.

B. Decoupling Procedure

Decoupling of the control problem into the two, simpler control problems of reference tracking and cell current balancing eliminates the need to consider interaction between these subsystems and instead, enables controllers to be designed independently, and to different specifications. To this end, a procedure for the decoupling of the reference tracking and current balancing subsystems will be demonstrated in this Section.

To achieve controller decoupling, an appropriate state transformation is required. The usual control strategy for active current balancing is based on average current sharing. Since active current balancing aims to minimize the difference between individual cell currents and the average current of the cells, a new state vector is proposed

$$\begin{aligned} \boldsymbol{z} &= \left[\, i_g \; v_c \; i_{avg} \,\middle|\, i_{avg}-i_1 \; i_{avg}-i_2 \; \ldots \; i_{avg}-i_n \,\right]^{\mathsf{T}} \\ &= \left[\, \boldsymbol{z}_{tra} \,\middle|\, \boldsymbol{z}_{bal} \,\right]^{\mathsf{T}} \end{aligned} \tag{12}$$

where

$$i_{\text{avg}} = \frac{1}{n}\sum_{k=1}^{n} i_k. \tag{13}$$

The new state vector has two subvectors labeled $\boldsymbol{z}_{\text{tra}}$ and $\boldsymbol{z}_{\text{bal}}$. The subvector $\boldsymbol{z}_{\text{tra}}$ gathers states which define tracking dynamics, while the subvector $\boldsymbol{z}_{\text{bal}}$ gathers states describing the cell current imbalance. From the definition of state vectors $\boldsymbol{x}$ and $\boldsymbol{z}$, the transformation matrix follows:

$$\boldsymbol{T} = \left[\begin{array}{c|c} \boldsymbol{I}_{2\times 2} & \\ \hline & \boldsymbol{t}_0 \\ & \boldsymbol{T}_0 \end{array}\right] \tag{14}$$

where

$$\boldsymbol{T}_0 = n^{-1}\cdot \boldsymbol{1}_{n\times n} - \boldsymbol{I}_{n\times n} \tag{15}$$

$$\boldsymbol{t}_0 = n^{-1}\cdot \boldsymbol{1}_{1\times n} \tag{16}$$

and the transformation matrix $\boldsymbol{T}$ defines the relation $\boldsymbol{z} = \boldsymbol{T}\boldsymbol{x}$ between the state vectors.

The transformation matrix $\boldsymbol{T}$ defined in (14) is not a square matrix. Consequently, the inverse transformation is not defined. To have the transformation matrix in a square form the following modification is proposed:

$$\boldsymbol{z} = \begin{bmatrix} \boldsymbol{T} & \boldsymbol{v} \end{bmatrix} \begin{bmatrix} \boldsymbol{x} \\ 0 \end{bmatrix} = \boldsymbol{H} \begin{bmatrix} \boldsymbol{x} \\ 0 \end{bmatrix} \tag{17}$$

where the vector

$$\boldsymbol{v} = \begin{bmatrix} 0 & 0 & 0 & \boldsymbol{1}_{1\times n} \end{bmatrix}^{\mathsf{T}} \tag{18}$$

is selected such that the norms of transformation matrices $\boldsymbol{T}$ and $\boldsymbol{H}$ remain the same, that is, $\|\boldsymbol{T}\|_\infty = \|\boldsymbol{H}\|_\infty$. The extended transformation matrix is consequently of the form

$$\boldsymbol{H} = \left[\begin{array}{c|cc} \boldsymbol{I}_{2\times 2} & & \\ \hline & \boldsymbol{t}_0 & 0 \\ & \boldsymbol{T}_0 & \boldsymbol{1}_{n\times 1} \end{array}\right]. \tag{19}$$

As $\boldsymbol{H}$ is square and nonsingular, the inverse transformation exists and is given by

$$\boldsymbol{H}^{-1} = \left[\begin{array}{c|cc} \boldsymbol{I}_{2\times 2} & & \\ \hline & \boldsymbol{1}_{n\times 1} & \boldsymbol{T}_0 \\ & 0 & \boldsymbol{t}_0 \end{array}\right]. \tag{20}$$

It is straightforward to check that $\boldsymbol{H}\boldsymbol{H}^{-1} = \boldsymbol{I}$. From (20) it follows that the inverse relationship between state vectors is given by $\boldsymbol{x} = \boldsymbol{H}^{-1}\boldsymbol{z}$, and consequently both direct and inverse transformations are defined.

To get a standard form of transformed state space model additional algebraic operations must be applied to the explicit model. Extending (8) by adding the zero vectors, a standard form is obtained. The complete transformation is defined as

$$\begin{bmatrix} \dot{\boldsymbol{x}} \\ 0 \end{bmatrix} = \left[\begin{array}{c|c} \boldsymbol{A} & \\ \hline & 0 \end{array}\right] \begin{bmatrix} \boldsymbol{x} \\ 0 \end{bmatrix} + \left[\begin{array}{c} \boldsymbol{B} \\ \hline \boldsymbol{0}_{1\times(n+1)} \end{array}\right] \boldsymbol{u}. \tag{21}$$

Substituting (17) into (21) the state-space model is transformed into

$$\boldsymbol{H}^{-1}\dot{\boldsymbol{z}} = \left[\begin{array}{c|c} \boldsymbol{A} & \\ \hline & 0 \end{array}\right] \boldsymbol{H}^{-1}\boldsymbol{z} + \left[\begin{array}{c} \boldsymbol{B} \\ \hline \boldsymbol{0}_{1\times(n+1)} \end{array}\right] \boldsymbol{u}. \tag{22}$$

Finally, by multiplying (22) on the LHS by $\boldsymbol{H}$, the new equation has the following form:

$$\dot{\boldsymbol{z}} = \boldsymbol{H} \left[\begin{array}{c|c} \boldsymbol{A} & \\ \hline & 0 \end{array}\right] \boldsymbol{H}^{-1}\boldsymbol{z} + \boldsymbol{H} \left[\begin{array}{c} \boldsymbol{B} \\ \hline \boldsymbol{0}_{1\times(n+1)} \end{array}\right] \boldsymbol{u}. \tag{23}$$

A similar transformation is required for the control inputs, in order to decouple the reference tracking control signal (supplied from the reference tracking controller) from the balancing control signal (responsible for cell current balancing). The following transformation is proposed:

$$\boldsymbol{u} = \boldsymbol{W}\boldsymbol{p} \tag{24}$$

where the matrix $\boldsymbol{W}$ is defined as

$$\boldsymbol{W} = \left[\begin{array}{c|c} 1 & \\ \hline \boldsymbol{1}_{n\times 1} & \boldsymbol{T}_0 \end{array}\right] \tag{25}$$

and the vector $\boldsymbol{p}$ represents the new control inputs defined as

$$\boldsymbol{p} = \left[\begin{array}{c} v_{\text{g}} \\ \hline u_{\text{tra}} \\ \hline u_{\text{tra}} - u_1 \\ u_{\text{tra}} - u_2 \\ \vdots \\ u_{\text{tra}} - u_n \end{array}\right] = \left[\begin{array}{c} v_{\text{g}} \\ \hline \boldsymbol{r}_{\text{tra}} \\ \hline \boldsymbol{r}_{\text{bal}} \end{array}\right] = \left[\begin{array}{c} v_{\text{g}} \\ \hline \boldsymbol{r} \end{array}\right]. \tag{26}$$

Consequently, $\boldsymbol{r}_{\text{tra}}$ is a control input vector used to drive states $[i_{\text{g}}\ v_{\text{c}}\ i_{\text{avg}}]$, while control input vector $\boldsymbol{r}_{\text{bal}}$ is used for balancing cell currents.

Applying (23) and the control input transformation (24), the state space model has the following form:

$$\dot{\boldsymbol{z}} = \boldsymbol{\mathcal{A}}\boldsymbol{z} + \boldsymbol{\mathcal{B}}\boldsymbol{p} \tag{27}$$

where $\boldsymbol{\mathcal{A}}$ and $\boldsymbol{\mathcal{B}}$ are defined as

$$\boldsymbol{\mathcal{A}} = \boldsymbol{H} \left[\begin{array}{c|c} \boldsymbol{A} & \\ \hline & 0 \end{array}\right] \boldsymbol{H}^{-1} \qquad \boldsymbol{\mathcal{B}} = \boldsymbol{H} \left[\begin{array}{c} \boldsymbol{B} \\ \hline \boldsymbol{0}_{1\times(n+1)} \end{array}\right] \boldsymbol{W}. \tag{28}$$

Following the matrix multiplications in (28)

$$\boldsymbol{\mathcal{A}} = \left[\begin{array}{ccc|c} -R_{\text{f}}L_{\text{f}}^{-1} & L_{\text{f}}^{-1} & 0 & \\ -C_{\text{f}}^{-1} & 0 & nC_{\text{f}}^{-1} & \\ 0 & \gamma & -nR\gamma & \\ \hline & & & -R\cdot\boldsymbol{\mathcal{C}} \end{array}\right] \tag{29}$$

$$\boldsymbol{\mathcal{B}} = \left[\begin{array}{cc|c} -L_{\text{f}}^{-1} & 0 & \\ 0 & 0 & \\ 0 & \gamma & \\ \hline & & \boldsymbol{\mathcal{C}} \end{array}\right] \tag{30}$$

where $\boldsymbol{\mathcal{C}} \in \mathbb{R}^{n\times n}$ is a circulant matrix defined by

$$\boldsymbol{\mathcal{C}} = \boldsymbol{T}_0\boldsymbol{\mathcal{L}}^{-1}\boldsymbol{T}_0. \tag{31}$$

The block diagonal form of $\boldsymbol{\mathcal{A}}$ and $\boldsymbol{\mathcal{B}}$ demonstrates that decoupling has been successfully achieved; that is, the tracking states $\boldsymbol{z}_{\text{tra}}$, and tracking control action u_{tra}, do not affect the balancing states $\boldsymbol{z}_{\text{bal}}$, and vice versa. This decoupling permits controllers for the reference tracking and cell current balancing tasks to be independently designed and analyzed. In other words, the placement of eigenvalues for each subsystem can be done in such a way that the specific requirements of each control problem are taken into account during the design process. This is particularly relevant for modular converters in which control may be distributed, or in cases where there are significant differences between the dynamics of the reference tracking and cell current balancing.

C. Decoupled Model Properties

The transformations proposed in Section III-B provide a method to decouple the original model into two subsystems. Before the decoupled model is applied to a controller design process, however, the fundamental properties of the model need to be verified, including checks for stability, controllability, and observability. The stability analysis is based on checking eigenvalues of the matrix $\boldsymbol{\mathcal{A}}$, while controllability and observability is tested against the rank of the controllability and observability matrices.

The matrix $\boldsymbol{\mathcal{A}}$ is block diagonal as a result of the state transformation and can be rewritten in the following form, which is convenient for exploring the fundamental properties:

$$\boldsymbol{\mathcal{A}} = \left[\begin{array}{c|c} \boldsymbol{\mathcal{A}}_{11} & \\ \hline & \boldsymbol{\mathcal{A}}_{22} \end{array}\right] \tag{32}$$

where $\boldsymbol{\mathcal{A}}_{11}$ and $\boldsymbol{\mathcal{A}}_{22}$ are defined as

$$\boldsymbol{\mathcal{A}}_{11} = \begin{bmatrix} -R_\mathrm{f}L_\mathrm{f}^{-1} & L_\mathrm{f}^{-1} & 0 \\ -C_\mathrm{f}^{-1} & 0 & nC_\mathrm{f}^{-1} \\ 0 & \gamma & -nR\gamma \end{bmatrix} \tag{33}$$

$$\boldsymbol{\mathcal{A}}_{22} = -R \cdot \boldsymbol{\mathcal{C}}. \tag{34}$$

For the purpose of the property analysis of model (27), the control matrix $\boldsymbol{\mathcal{B}}$ needs to be rewritten as the block matrix

$$\boldsymbol{\mathcal{B}} = \left[\mathring{\boldsymbol{\mathcal{B}}} \;\middle|\; \tilde{\boldsymbol{\mathcal{B}}}\right]. \tag{35}$$

Matrices $\mathring{\boldsymbol{\mathcal{B}}}$ and $\tilde{\boldsymbol{\mathcal{B}}}$ are defined as

$$\mathring{\boldsymbol{\mathcal{B}}} = \begin{bmatrix} -L_f^{-1} \\ \mathbf{0}_{(n+2)\times 1} \end{bmatrix} \tag{36}$$

$$\tilde{\boldsymbol{\mathcal{B}}} = \left[\begin{array}{c|c} \tilde{\boldsymbol{\mathcal{B}}}_{11} & \\ \hline & \tilde{\boldsymbol{\mathcal{B}}}_{22} \end{array}\right] \tag{37}$$

where partitions $\tilde{\boldsymbol{\mathcal{B}}}_{11}$ and $\tilde{\boldsymbol{\mathcal{B}}}_{22}$ are given below

$$\tilde{\boldsymbol{\mathcal{B}}}_{11} = \begin{bmatrix} \mathbf{0}_{2\times 1} \\ \gamma \end{bmatrix} \tag{38}$$

$$\tilde{\boldsymbol{\mathcal{B}}}_{22} = \boldsymbol{\mathcal{C}}. \tag{39}$$

The upper block $\boldsymbol{\mathcal{A}}_{11}$ has all eigenvalues negative and subsequently is stable. From the definitions (15) and (31), it follows that lower block $\boldsymbol{\mathcal{A}}_{22}$ is rank deficient with rank $n-1$, and consequently has one zero eigenvalue. Checking the rank of controllability matrices

$$\boldsymbol{\mathcal{R}}_{11} = \begin{bmatrix} \tilde{\boldsymbol{\mathcal{B}}}_{11} & \boldsymbol{\mathcal{A}}_{11}\tilde{\boldsymbol{\mathcal{B}}}_{11} & \boldsymbol{\mathcal{A}}_{11}^2\tilde{\boldsymbol{\mathcal{B}}}_{11} & \ldots & \boldsymbol{\mathcal{A}}_{11}^{(n+2)}\tilde{\boldsymbol{\mathcal{B}}}_{11} \end{bmatrix} \tag{40}$$

$$\boldsymbol{\mathcal{R}}_{22} = \begin{bmatrix} \tilde{\boldsymbol{\mathcal{B}}}_{22} & \boldsymbol{\mathcal{A}}_{22}\tilde{\boldsymbol{\mathcal{B}}}_{22} & \boldsymbol{\mathcal{A}}_{22}^2\tilde{\boldsymbol{\mathcal{B}}}_{22} & \ldots & \boldsymbol{\mathcal{A}}_{22}^{(n+2)}\tilde{\boldsymbol{\mathcal{B}}}_{22} \end{bmatrix} \tag{41}$$

it follows that $\boldsymbol{\mathcal{R}}_{11}$ is full rank while $\boldsymbol{\mathcal{R}}_{22}$ is rank deficient due to $\boldsymbol{\mathcal{A}}_{22}$. This means that the states $\boldsymbol{z}_\mathrm{tra}$ are fully controllable, while the states $\boldsymbol{z}_\mathrm{bal}$ have one uncontrollable eigenvalue.

The analysis of the uncontrollable mode, i.e., the zero eigenvalue, of matrix $\boldsymbol{\mathcal{A}}_{22}$ requires checking the solutions of $\boldsymbol{\mathcal{A}}_{22}\boldsymbol{z}_\mathrm{bal} = \mathbf{0}_{n\times 1}$. As $\boldsymbol{\mathcal{A}}_{22}$ is circulant, the solution to this equation is of the form $\boldsymbol{z}_\mathrm{bal} = [\xi\ \xi\ \ldots\ \xi]^\mathsf{T}$. Based on definition (12), the only valid solution case is $\xi = 0$, which corresponds to the null state. Consequently this uncontrollable mode is not of concern.

For a more compact notation, the model (27), given (12), (24), (32), and (35), can be rewritten as

$$\begin{bmatrix} \dot{\boldsymbol{z}}_\mathrm{tra} \\ \dot{\boldsymbol{z}}_\mathrm{bal} \end{bmatrix} = \left[\begin{array}{c|c} \boldsymbol{\mathcal{A}}_{11} & \\ \hline & \boldsymbol{\mathcal{A}}_{22} \end{array}\right] \begin{bmatrix} \boldsymbol{z}_\mathrm{tra} \\ \boldsymbol{z}_\mathrm{bal} \end{bmatrix} + \left[\begin{array}{c|c} \tilde{\boldsymbol{\mathcal{B}}}_{11} & \\ \hline & \tilde{\boldsymbol{\mathcal{B}}}_{22} \end{array}\right] \begin{bmatrix} \boldsymbol{r}_\mathrm{tra} \\ \boldsymbol{r}_\mathrm{bal} \end{bmatrix}. \tag{42}$$

Given the diagonal form of matrix $\tilde{\boldsymbol{\mathcal{B}}}$, the control input $\boldsymbol{r}$ can be substituted by the following state feedback:

$$\boldsymbol{r} = -\boldsymbol{K}\boldsymbol{z} = \left[\begin{array}{c|c} \boldsymbol{K}_\mathrm{tra} & \\ \hline & \boldsymbol{K}_\mathrm{bal} \end{array}\right] \tag{43}$$

where $\boldsymbol{K}_\mathrm{tra} \in \mathbb{R}^{3\times 1}$ and $\boldsymbol{K}_\mathrm{bal} \in \mathbb{R}^{n\times n}$ are gain matrices. The matrix $\boldsymbol{K}_\mathrm{tra}$ can be designed to satisfy the required tracking performance, while $\boldsymbol{K}_\mathrm{bal}$ is a matrix whose values determine the performance of the balancing controller. Substituting (43) into (42) yields

$$\begin{bmatrix} \dot{\boldsymbol{z}}_\mathrm{tra} \\ \dot{\boldsymbol{z}}_\mathrm{bal} \end{bmatrix} = \left[\begin{array}{c|c} \boldsymbol{\mathcal{A}}_{11} - \tilde{\boldsymbol{\mathcal{B}}}_{11}\boldsymbol{K}_\mathrm{tra} & \\ \hline & \boldsymbol{\mathcal{A}}_{22} - \tilde{\boldsymbol{\mathcal{B}}}_{22}\boldsymbol{K}_\mathrm{bal} \end{array}\right] \begin{bmatrix} \boldsymbol{z}_\mathrm{tra} \\ \boldsymbol{z}_\mathrm{bal} \end{bmatrix}. \tag{44}$$

IV. APPLICATION OF THE DECOUPLED MODEL TO CONTROLLER DESIGN

To demonstrate the advantage of the decoupling methodology presented in this article to the controller design process for a paralleled interleaved converter, the decoupled model developed in Section III will be applied to design reference tracking and current balancing controllers for a practical converter. The key contribution of this article is enabling the reference tracking and balancing controllers to be independently designed, and consequently, dynamics of the resulting closed-loop systems to be independently specified; this process will be demonstrated explicitly in this section. The intent of this section is therefore not to make a direct comparison with the dynamic performance of existing controllers documented in the literature, but rather, to validate the effectiveness and salient advantages of the decoupled design methodology.

It should be noted that the decoupled model developed in this article is applicable independent of any specific control design technique; any state-space technique may be used to design a control law based on the decoupled model (e.g., the

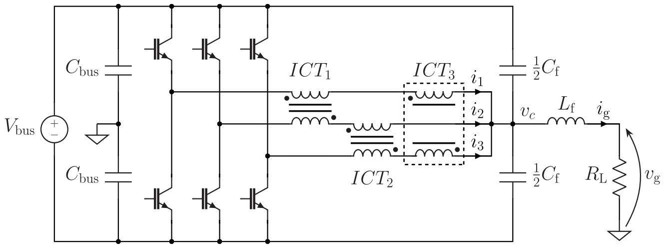

Fig. 3. Circuit diagram of the experimental prototype showing output filter configuration, including cyclic cascade network comprising three ICTs.

TABLE I
COMPONENT VALUES FOR EXPERIMENTAL PROTOTYPE

Symbol	Component	Value
C_{bus}	DC bus capacitance	14.1 mF
L_{lk}	ICT leakage inductance	313 µH
L_{m}	ICT magnetizing inductance	831 µH
R_{ICT}	ICT equivalent series resistance	50 mΩ
C_{f}	Filter capacitance	50 µF
L_{f}	Output inductance	1.2 mH
R_{f}	Output inductor ESR	7 mΩ
R_{L}	Load resistance	11 Ω

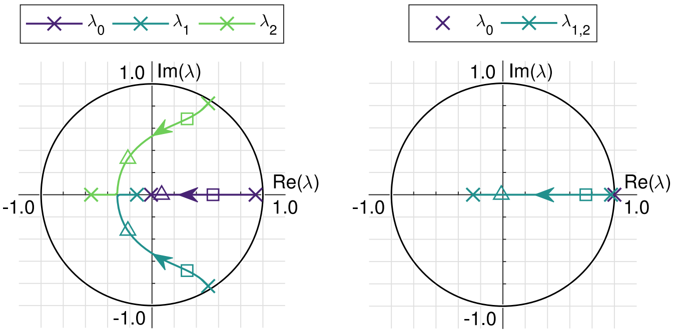

(a) (b)

Fig. 4. Trajectories of closed-loop eigenvalues for decreasing values of $\rho \in [1{\times}10^{-7}, 1{\times}10^{0}]$ for (a) reference tracking controller and (b) balancing controller. □ and △ denote, respectively, a "relaxed" (low feedback gain) and "aggressive" (high feedback gain) design point for each controller.

TABLE II
CONTROLLER DESIGN PARAMETERS AND RESULTING FEEDBACK GAINS

	ρ_{tra}	$\boldsymbol{K}_{\mathrm{tra}}$	ρ_{bal}	$\mathcal{K}_{\mathrm{bal}}$
□	$7.40\mathrm{E}^{-4}$	[4.70 0.230 5.44]	$2.74\mathrm{E}^{-5}$	5.49
△	$1.09\mathrm{E}^{-2}$	[18.8 1.76 11.2]	$1.45\mathrm{E}^{-4}$	21.9

dead-beat control strategy proposed in [1] could be applied to design a balancing controller using the decoupled model). For the purposes of this example design, we select the LQR design technique, which guarantees an infinite gain margin, phase margin of at least 60°, and is tolerant to input nonlinearities bounded on $(0.5, 2)$ [21].

An LQR design requires specification of the weighting matrices $\boldsymbol{Q}$ and $\boldsymbol{R}$ to minimize the quadratic cost function, where $\boldsymbol{Q}$ determines the relative penalty for state errors, while $\boldsymbol{R}$ determines the penalty for control action. For the tracking controller, we select i_g as the quantity of interest, and assign no priority to the other states, resulting in $\boldsymbol{Q}_{\mathrm{tra}} = \mathrm{diag}(1, 0, 0)$. For the balancing controller, given the symmetry in the converter topology, we assign equal weighting to $i_1 \ldots i_n$ such that $\boldsymbol{Q}_{\mathrm{bal}} = \boldsymbol{I}_{n\times n}$. Similarly, control action can also be penalized equally, such that $\boldsymbol{R} = \rho{\cdot}\boldsymbol{I}$, where the value of ρ can be independently selected for the tracking and balancing controllers, and decreasing values of ρ will result in increasing feedback gains.

As a practical example, the abovementioned design methodology is applied to the experimental 3-cell converter depicted in Fig. 3, which features a cyclic cascade coupling network. Numeric values for matrices $\boldsymbol{\mathcal{A}}$ and $\boldsymbol{\mathcal{B}}$ are determined from the experimental converter component values provided in Table I, where

$$L = 2(L_{\mathrm{lk}} + L_{\mathrm{m}}) \tag{45}$$

$$M = L_{\mathrm{m}} \tag{46}$$

$$R = 2R_{\mathrm{ICT}}. \tag{47}$$

As the control law will ultimately be implemented on a digital system, the sample rate, T_s, must also be specified; a sample rate of 96 μs is selected, commensurate with the switching frequency of the experimental prototype, 10.4 kHz. Feedback gains for the two controllers are calculated using the MATLAB function `lqrd` as follows:

$$\boldsymbol{K}_{\mathrm{tra}} = \mathtt{lqrd}\left(\boldsymbol{A}_{\mathrm{tra}}, \boldsymbol{B}_{\mathrm{tra}}, \boldsymbol{Q}_{\mathrm{tra}}, \boldsymbol{R}_{\mathrm{tra}}, T_s\right) \tag{48}$$

$$\boldsymbol{K}_{\mathrm{bal}} = \mathtt{lqrd}\left(\boldsymbol{A}_{\mathrm{bal}}, \boldsymbol{B}_{\mathrm{bal}}, \boldsymbol{Q}_{\mathrm{bal}}, \boldsymbol{R}_{\mathrm{bal}}, T_s\right). \tag{49}$$

It should be noted that the resulting gain matrix $\boldsymbol{K}_{\mathrm{bal}}$ is of the form $\mathrm{circ}(2\kappa, -\kappa, -\kappa)$, and from the definitions (12) and (13) it can be trivially shown that $\boldsymbol{K}_{\mathrm{bal}}$ can be simplified to $\mathcal{K}_{\mathrm{bal}} = 3\kappa$ such that $\boldsymbol{K}_{\mathrm{bal}}\boldsymbol{z}_{\mathrm{bal}} = \mathcal{K}_{\mathrm{bal}}{\cdot}\boldsymbol{z}_{\mathrm{bal}}$.

The dynamics of the resulting closed-loop control law are determined by the selection of values of ρ for the balancing and tracking controllers. Fig. 4 shows the trajectories of the closed-loop eigenvalues as the design parameter ρ is varied for each of the controllers. To demonstrate the utility of the decoupled design methodology, we design independently for each of the controllers an "aggressive" (high feedback gains) and "relaxed" (low feedback gains) control law by selecting appropriate values for ρ_{tra} and ρ_{bal}. The resulting feedback gains are summarized in Table II and the corresponding closed-loop eigenvalues are plotted in Fig. 4, where □ and △ denote the low and high feedback gain designs, respectively. These controller designs will be applied experimentally in Section V to validate that decoupling of the reference tracking and balancing controllers has been achieved.

V. EXPERIMENTAL VALIDATION

To validate the proposed technique for decoupling of active current balancing and reference tracking control tasks, an experimental prototype (see Fig. 3) was developed and the closed-loop controllers designed in Section IV were implemented. In this section, transient performance of the reference tracking and balancing controllers is investigated to validate that the closed-loop performance of these systems is truly decoupled as predicted by the control design methodology developed in this article.

It is demonstrated in this section that the dynamic performance of the reference tracking and balancing subsystems is determined solely by the respective controller; that is, modification of the balancing controller design does not affect the reference tracking performance, and vice versa. In the following subsections, the hardware prototype is described and experimental results are presented and discussed.

A. Hardware Prototype

The experimental prototype comprised a three phase-leg, SEMIKRON SEMIKUBE IGBT-based VSI with split-bus configuration, driving a single phase, resistive load. The load was returned to the dc bus midpoint. A dc power supply was used to regulate the dc bus of the VSI to 400 V. The prototype supplied a fixed 11 Ω resistive load.

The three phase legs of the VSI were coupled to the load via an *LCL* filter, which included a cyclic cascade network of ICTs on the VSI side of the filter. Leakage and magnetizing inductances were calculated for each of the ICTs using open- and short-circuit measurements taken using an *LCR* meter; for the purposes of this experimental validation, the mean value of these parameters were used. The values of all passive components used in the hardware prototype are documented in Table I.

Modulation, sampling, and filtering were conducted in an field programmable gate array (FPGA)-based data acquisition and control system [22], while the active balancing control and open-loop reference were calculated in a Real-Time Digital Simulation (RTDS) real-time simulator. The switching frequency of the converter was configured to 10.4 kHz ($T_{\mathrm{PWM}} = 96\ \mu$s) with a phase shift of 120° applied between phase legs. A phase accumulated carrier pulsewidth modulation (PWM) strategy [23] with 32-bit phase accumulator, 16-bit precision compare value, zero-order hold, and multiple-edge lockout circuit was employed for the PWM. All voltages and currents in the prototype were sampled at 1 MHz, and a 96-sample moving average filter was applied to attenuate harmonics at the switching frequency and its multiples. Measurements were subsequently decimated to the 5 μs time step at which the control actions were calculated and applied. A photo of the experimental prototype is shown in Fig. 5 and a detailed discussion of the experimental instrumentation and control platform is provided in [22].

The control action for the experimental converter was calculated by

$$u_n = u_{\mathrm{ff}} - \boldsymbol{K}_{\mathrm{tra}}\left(\boldsymbol{z}_{\mathrm{tra}} - \boldsymbol{z}^*_{\mathrm{tra}}\right) - \mathcal{K}_{\mathrm{bal}}\left(i_n - i_{\mathrm{avg}}\right) \tag{50}$$

given

$$i^*_{\mathrm{g}} = 3i^*_{\mathrm{avg}} = I_{\mathrm{g}}\sin(\omega t + \phi) \tag{51}$$

$$v^*_{\mathrm{c}} = v_{\mathrm{g}} + R_{\mathrm{f}} i^*_{\mathrm{g}} + L_{\mathrm{f}}\frac{\mathrm{d}i^*_{\mathrm{g}}}{\mathrm{d}t} \tag{52}$$

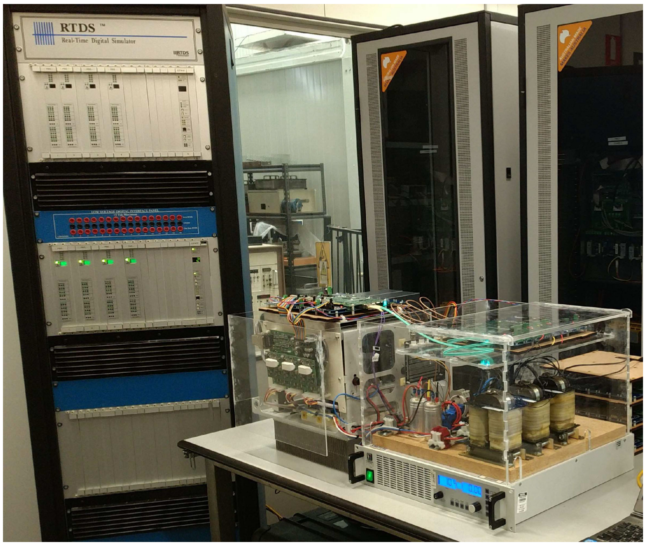

Fig. 5. Photo of the experimental prototype showing real-time simulator, three-phase-leg inverter module, and output filter network (left to right).

$$u_{\mathrm{ff}} = v_{\mathrm{g}} + \left(R_{\mathrm{f}} + \frac{R}{3}\right) i^*_{\mathrm{g}} + \left(L_{\mathrm{f}} + \frac{2L_{\mathrm{lk}}}{3}\right)\frac{\mathrm{d}i^*_{\mathrm{g}}}{\mathrm{d}t} \tag{53}$$

where I_{g} is the amplitude of a sinusoidal load current reference having arbitrary phase ϕ, and frequency $\omega = 100\ \pi$. The control architecture is depicted in Fig. 6.

As the units of u_n are $[V]$, mapping of the control action to modulation depth is performed by assuming a fixed bus voltage such that the modulation depth for each phase leg can be calculated by

$$m_n = \frac{2}{V_{\mathrm{bus}}} u_n, \qquad m_n \in [-1, 1]. \tag{54}$$

A small amount of artificial imbalance was introduced in the form of a 0.1% dc offset to one of the three phase legs (phase-leg C) modulation depths, to produce an observable amount of imbalance in the output currents. Note that this represents a 96 ns asymmetry in switching times between phase legs, which is not unreasonable when considering typical timing uncertainties in gate drive signal pathways.

B. Experimental Results

To examine the dynamics of the designed balancing and tracking controllers, a step change of 9 to 0.9 $\mathrm{A_{RMS}}$ was applied to the 50 Hz output current reference at $t = 0$ s. Fig. 7 shows the resulting output current and phase-leg currents with low tracking gain and low balancing gain controller variants implemented. Good balancing and tracking performance is demonstrated.

To validate that decoupling has been achieved the experiment was repeated with all combinations of tracking and balancing controller design points. Figs. 8 and 9 show the transient tracking and balancing performance, respectively, for different controller combinations.

Fig. 8 clearly shows that reference tracking performance is unaffected by the choice of balancing controller design point, and is

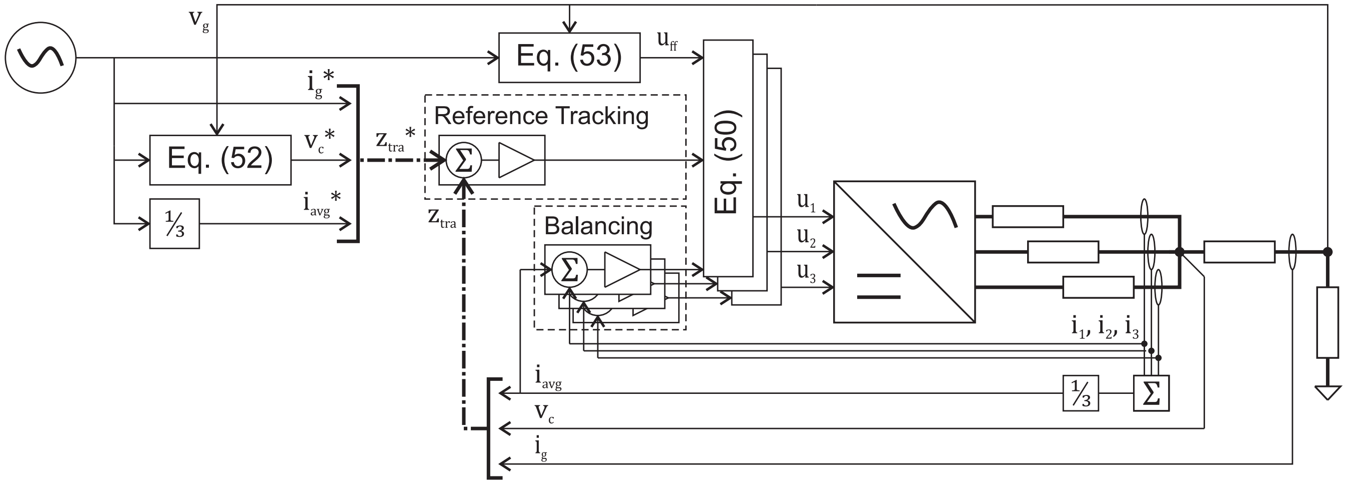

Fig. 6. Block diagram showing architecture of the decoupled controller applied to the experimental prototype.

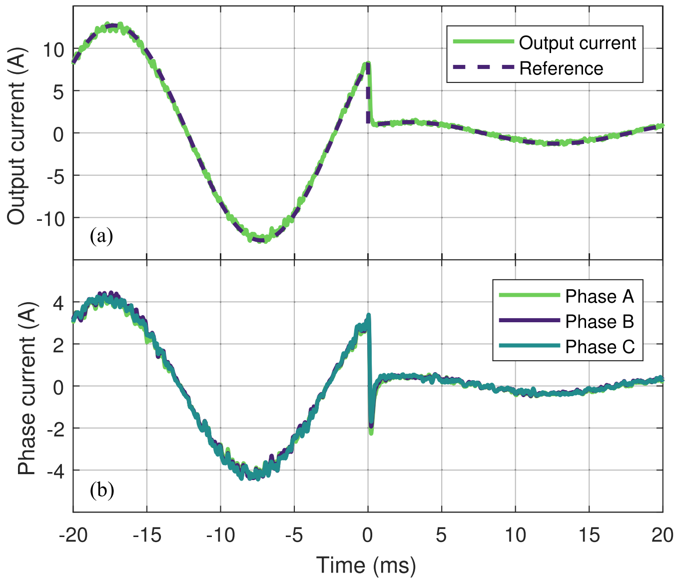

Fig. 7. Plots of (a) load current and (b) phase-leg current for a step change in reference current from 9 to 0.9 $\mathrm{A_{RMS}}$. Waveforms shown are for the low tracking gain, low balancing gain controller design point.

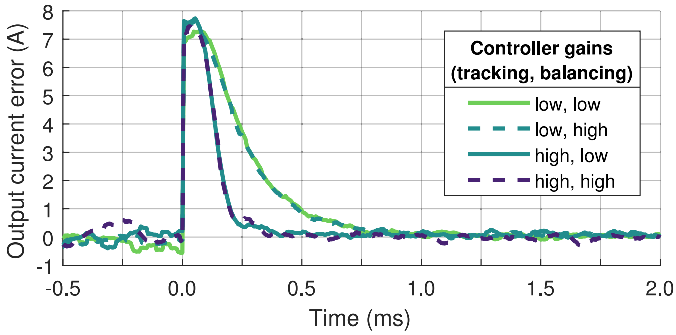

Fig. 8. Plot of output current tracking error for a step change in reference current from 9 to 0.9 $\mathrm{A_{RMS}}$, for all combinations of tracking and balancing controller design points.

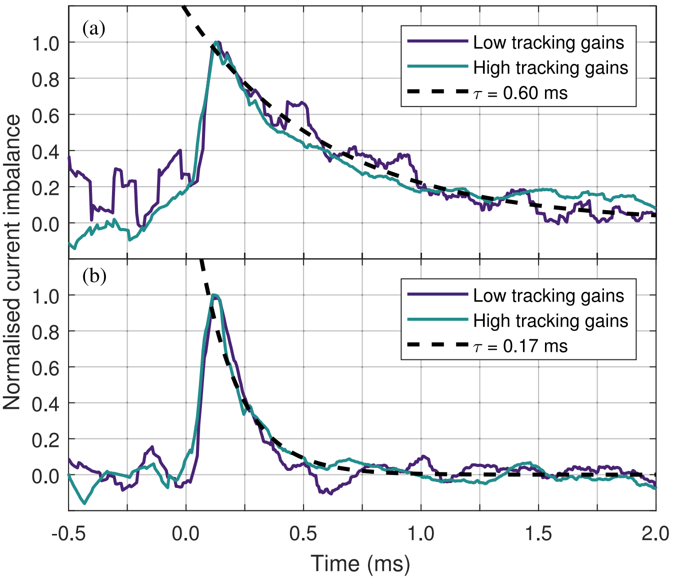

Fig. 9. Plot of current imbalance transient for one output phase for the (a) low gain balancing controller design and (b) high gain balancing controller design. Current imbalance is normalized to the peak transient current imbalance for each case. For each balancing controller design point, a first-order exponential line of best fit has been shown, with corresponding time constant indicated in the legend.

dependent only on the design of the reference tracking controller. The plot also validates the design methodology presented in Section IV, with the transient response time reduced from ~750 to ~250 μs, comparing the low-gain and high-gain tracking controller designs, respectively. Similarly, Fig. 9 demonstrates that transient balancing performance is unaffected by the choice of tracking controller design, with the time constant of the balancing transient independent of the selected tracking controller gains. An improvement in the balancing time constant from ~600 to ~170 μs is demonstrated, comparing the low-gain and high-gain balancing controller designs, respectively.

These data validate that the decoupling of reference tracking and balancing control tasks via the methodology presented in Section III is achievable in practice, such that controller performance can be independently designed and analyzed as demonstrated in Section IV.

VI. CONCLUSION

This article presents a methodology for the decoupling of the current balancing and reference tracking control problems in multicell, paralleled converters. This decoupling process allows the balancing and reference tracking controllers to be designed and analyzed independently, such that the dynamics of neither subsystem need be compromised. The proposed methodology is shown to be generally applicable to symmetrical, n-cell paralleled converter topologies featuring uncoupled or coupled output inductor networks.

The presented decoupling and controller design methodologies have been validated experimentally at 100 $\mathrm{V_{RMS}}$ and 9 $\mathrm{A_{RMS}}$, using a three-cell parallel interleaved converter with cyclic cascade coupled inductor filter network. The implemented balancing control is effective in minimizing intercell current imbalance. Decoupling has been explicitly demonstrated experimentally, with dynamic tracking performance unaffected by choice of balancing controller design, and vice versa.

APPENDIX
COUPLING MATRIX DEFINITIONS AND PROPERTIES

In Section II, we introduce a matrix $\boldsymbol{\mathcal{L}}$, denoted as the "coupling matrix," which defines the inductive coupling network between the converter cells and the PCC. In the general case, this matrix takes the following form:

$$\boldsymbol{\mathcal{L}} = \begin{bmatrix} L_1 & -M_{12} & -M_{13} & \dots & -M_{1n} \\ -M_{12} & L_2 & -M_{23} & \dots & -M_{2n} \\ -M_{13} & -M_{23} & L_3 & \ddots & -M_{3n} \\ \vdots & \vdots & \ddots & \ddots & \vdots \\ -M_{1n} & -M_{2n} & -M_{3n} & \dots & L_n \end{bmatrix} \tag{55}$$

where L_j is the total self-inductance of phase-leg j, and M_{jk} is the mutual inductance between phase-legs j and k. If a symmetrical coupling network is assumed such that

$$L_j = L, \qquad j \in [1, n] \tag{56}$$

$$M_{jk} \in \{M, 0\}, \qquad j, k \in [1, n], \quad j \neq k \tag{57}$$

the matrix $\boldsymbol{\mathcal{L}}$ can be further simplified, and, as will be subsequently shown, always takes the form of a circulant matrix. For the purposes of this article, we will define the coupling matrix for the three salient coupling network classes identified from the literature, namely, uncoupled, multicoupled, and cyclic cascade.

A. Uncoupled case

The uncoupled case is the simplest and occurs when no mutual coupling exists between phase legs. In this case, (55) reduces to

$$\boldsymbol{\mathcal{L}}_{\mathrm{uc}} = L \cdot \boldsymbol{I}_{n\times n}. \tag{58}$$

B. Multicoupled Case

The multicoupled case arises for symmetrical coupling networks formed via a common multileg magnetic core (multi-interphase transformers), or via the combinatorial cascade or whiffletree topologies (constructed from multiple two-winding interphase transformers) [1], [10]. All of these topologies have been shown to result in the same equivalent inductance, such that (55) simplifies to

$$\boldsymbol{\mathcal{L}}_{\mathrm{mc},n\times n} = \mathrm{circ}\left(L, -M, \dots, -M\right) \tag{59}$$

where the circ operator produces a circulant matrix with first row equal to the operand. It is important to note that the ratio of M to L is bounded by the case of perfect coupling [1] such that

$$\frac{M}{L} < \frac{1}{n-1} \tag{60}$$

and consequently $\boldsymbol{\mathcal{L}}_{\mathrm{mc}}$ is strictly diagonally dominant.

C. Cyclic Cascade Case

The cyclic cascade topology results in a symmetrical coupling network in which mutual coupling only exists between adjacent phase legs. For $n \leqslant 3$, this results in a coupling matrix, which is equivalent to the multicoupled case, however, for $n > 3$ some zero elements are present in the coupling matrix, such that

$$\boldsymbol{\mathcal{L}}_{\mathrm{cc},n\times n} = \mathrm{circ}\left(L, -M, 0, \dots, 0, -M\right), \qquad n > 3. \tag{61}$$

Similar to the multicoupled case, the ratio of M to L for the cyclic cascade topology is bounded by perfect coupling [1]

$$\frac{M}{L} < \frac{1}{2} \tag{62}$$

which guarantees that $\boldsymbol{\mathcal{L}}_{\mathrm{cc}}$ is strictly diagonally dominant.

REFERENCES

[1] G. J. Capella, J. Pou, S. Ceballos, J. Zaragoza, and V. G. Agelidis, "Current-balancing technique for interleaved voltage source inverters with magnetically coupled legs connected in parallel," *IEEE Trans. Ind. Electron.*, vol. 62, no. 3, pp. 1335–1344, Mar. 2015.

[2] J. S. S. Prasad and G. Narayanan, "Minimization of grid current distortion in parallel-connected converters through carrier interleaving," *IEEE Trans. Ind. Electron.*, vol. 61, no. 1, pp. 76–91, Jan. 2014.

[3] T. Itkonen, J. Luukko, and R. Pollanen, "Analysis of current characteristics of parallel three-phase voltage source inverters," in *Proc. 13th Eur. Conf. Power Electron. Appl.*, Sep. 2009, pp. 1–10.

[4] D. Floricau, E. Floricau, and G. Gateau, "New multilevel converters with coupled inductors: Properties and control," *IEEE Trans. Ind. Electron.*, vol. 58, no. 12, pp. 5344–5351, Dec. 2011.

[5] I. W. Jaskulski, H. Pinheiro, and L. Mariotto, "Multi-leg voltage source converter for grid connected wind turbines," in *Proc. Int. Conf. Clean Elect. Power*, May 2007, pp. 229–235.

[6] M. A. Abusara and S. M. Sharkh, "Design and control of a grid-connected interleaved inverter," *IEEE Trans. Power Electron.*, vol. 28, no. 2, pp. 748–764, Feb. 2013.

[7] Y. J. Ko, K. B. Lee, D. C. Lee, and J. M. Kim, "Fault diagnosis of three-parallel voltage-source converter for a high-power wind turbine," *IET Power Electron.*, vol. 5, no. 7, pp. 1058–1067, Aug. 2012.

[8] S. Sanchez, F. Richardeau, and D. Risaletto, "Design and fault-operation analysis of a modular cyclic cascade inter-cell transformer (ICT) for parallel multicell converters," *Math. Comput. Simul.*, vol. 131, no. Supplement C, pp. 190–199, 2017.

[9] B. M. H. Jassim, D. J. Atkinson, and B. Zahawi, "Modular current sharing control scheme for parallel-connected converters," *IEEE Trans. Ind. Electron.*, vol. 62, no. 2, pp. 887–897, Feb. 2015.

[10] I. G. Park and S. I. Kim, "Modeling and analysis of multi-interphase transformers for connecting power converters in parallel," in *Proc. PESC97. Rec. 28th Annu. IEEE Power Electron. Specialists Conf.*, Jun. 1997, vol. 2, pp. 1164–1170.

[11] A. M. Roslan, K. H. Ahmed, S. J. Finney, and B. W. Williams, "Improved instantaneous average current-sharing control scheme for parallel-connected inverter considering line impedance impact in microgrid networks," *IEEE Trans. Power Electron.*, vol. 26, no. 3, pp. 702–716, Mar. 2011.

[12] H. M. Hsieh, T. F. Wu, Y. E. Wu, H. S. Nien, and Y. E. Wu, "A compensation strategy for parallel inverters to achieve precise weighting current distribution," in *Proc. 40th IAS Annu. Meet. Conf. Rec. Ind. Appl. Conf.*, Oct. 2005, vol. 2, pp. 954–960.

[13] C. Wen, J. Li, X. Zhu, and H. Xu, "Research on circulation of parallel three-phase converters in MW wind power system," in *Proc. Workshop Power Electron. Intell. Transp. Syst.*, Aug. 2008, pp. 349–354.

[14] M. Yu *et al.*, "A novel decoupled current-sharing scheme based on circulating-impedance in parallel multi-inverter system," in *Proc. 33rd Annu. Conf. IEEE Ind. Electron. Soc.*, Nov. 2007, pp. 1668–1672.

[15] M. Xie, Y. Li, K. Cai, P. Wang, and X. Sheng, "A novel controller for parallel operation of inverters based on decomposing of output current," in *Proc. 40th IAS Annu. Meet. Conf. Rec. Ind. Appl. Conf.*, Oct. 2005, vol. 3, pp. 1671–1676.

[16] Y. K. Chen, T. F. Wu, Y. E. Wu, and C. P. Ku, "A current-sharing control strategy for paralleled multi-inverter systems using microprocessor-based robust control," in *Proc. IEEE Region 10 Int. Conf. Elect. Electron. Technol.*, 2001, vol. 2, pp. 647–653.

[17] J. Burkard, M. Pfister, and J. Biela, "Control concept for parallel interleaved three-phase converters with decoupled balancing control," in *Proc. 20th Eur. Conf. Power Electron. Appl.*, Sep. 2018, pp. 1–9.

[18] T. Meynard, B. C. Laplace, F. Forest, and E. Laboure, "Parallel multicell converters for high current: Design of intercell transformers," in *Proc. IEEE Int. Conf. Ind. Technol.*, Mar. 2010, pp. 1359–1364.

[19] E. Laboure, A. Cuniere, T. A. Meynard, F. Forest, and E. Sarraute, "A theoretical approach to intercell transformers, application to interleaved converters," *IEEE Trans. Power Electron.*, vol. 23, no. 1, pp. 464–474, Jan. 2008.

[20] X. Sun, Y.-S. Lee, and D. Xu, "Modeling, analysis, and implementation of parallel multi-inverter systems with instantaneous average-current-sharing scheme," *IEEE Trans. Power Electron.*, vol. 18, no. 3, pp. 844–856, May 2003.

[21] B. D. O. Anderson and J. B. Moore, *Optimal Control: Linear Quadratic Methods*. Upper Saddle River, NJ, USA: Prentice-Hall, 1990.

[22] M. A. H. Broadmeadow, G. R. Walker, and G. F. Ledwich, "A modular and scalable control and data acquisition system for power hardware in the loop (PHIL) amplifiers," in *Proc. 9th IET Int. Conf. Power Electron., Mach. Drives*, Apr. 2018, pp. 1–6.

[23] M. A. H. Broadmeadow, E. J. Burstinghaus, G. R. Walker, and G. F. Ledwich, "FPGA implementation of an arbitrary resample rate, first order hold (FOH), pulse width modulator," in *Proc. 9th IET Int. Conf. Power Electron., Mach. Drives*, Apr. 2018, pp. 1–6.